X^- (X = O, S, Se) Ions in Alkali Halide Lattices through Density Functional Calculations. 2. Interstitial Defect Models

V. Van Speybroeck,[†] F. Stevens,[†,‡] E. Pauwels,[†] H. Vrielinck,[‡] F. Callens,[‡] and M. Waroquier*[,†]

Center for Molecular Modeling, Laboratory of Theoretical Physics, Ghent University, Proeftuinstraat 86, B-9000 Ghent, Belgium, and Department of Solid State Sciences, Ghent University, Krijgslaan 281-S1, B-9000 Ghent, Belgium

Received: December 2, 2005; In Final Form: February 9, 2006

Density functional theory techniques are used to investigate the defect structure of X^- (X = O, S, Se) ions in MZ (M = Na, K, Rb and Z = Cl, Br) alkali halides which exhibit monoclinic-I *g*-tensor symmetry, using cluster in vacuo, embedded cluster, and periodic embedding schemes. Although a perturbed interstitial defect model was suggested from electron paramagnetic resonance experiments (EPR), the nature of the perturbation is still unknown. An appropriate defect model is developed theoretically by comparing structural and energetical properties of various defect configurations. Further validation is achieved by cross referencing experimental and computed EPR data. On the basis of the computational results, the following defect model is proposed: the X^- ion is located interstitially with a charge compensating halide vacancy in its first coordination shell.

1. Introduction

Defects introduced in chalcogen-doped alkali halide lattices exhibit a characteristic luminescence with a vibrational structure in the visible region.[1−3] Electron magnetic resonance techniques have proved to be an excellent tool to study mono- (X^-, X = O, S, Se), di- (X_2^-), and triatomic (X_3^-) chalcogen defects in alkali halides.[4−14] However, the exact defect structure for most configurations could not be determined from these experiments. Recently, the di-[15−18] and triatomic[19−20] defect structures were investigated theoretically using density functional theory (DFT) techniques.

In this work, we focus on the monoatomic chalcogen defects. As stated in the work of Maes et al.,[12] a distinction can be made between X^- centers where the chalcogen ion takes a substitutional or an interstitial position in the lattice. In a previous paper of the authors, hereafter referred to as 1, attention was focused on substitutional monoatomic chalcogen defects. This second part deals with interstitial monoatomic chalcogen centers in alkali halide lattices. The principal aim is to interpret the available electron paramagnetic resonance (EPR) data by cross referencing with theoretical calculations and to assign the appropriate defect model.

Whereas apparently only O^- and S^- can be introduced on substitutional positions in MZ lattices, O^-, S^-, and Se^- centers with monoclinic-I *g*-tensor symmetry have been reported but only in MCl lattices[6−12] and possibly also in KBr (O^-, see paper 1). The largest *g* value, that is, g_x, was observed along a ⟨110⟩ direction, whereas the g_y and g_z axes, corresponding to the intermediate and smallest *g* value, respectively, were tilted in the (110) plane by an angle α (Figure 1). This tilting angle is defined as the angle between the principal *g*-tensor axes in the (110) plane and the $\langle 1\bar{1}0\rangle$ and ⟨001⟩ principal axes. The principal axes of the hyperfine tensors were found to coincide within experimental error with those of the *g* tensor, although this is not imposed by symmetry. X^- centers of this class have been attributed to an interstitial X^- ion in a perturbed double tetrahedral environment.[10] It must be noted that this hypothesis could not be substantiated by superhyperfine data: no electron nuclear double resonance experiments could be performed due to the lack of saturation. Furthermore, accommodation problems for the larger Se^- ions in the smaller lattices were expected, due to the limited space in the interstitial cavity, and the nature of the perturbation could not be established experimentally.

The origin of the tilting of the *g* and hyperfine tensor axes in the case of an unperturbed interstitial X^- ion is not clear. Because different doping procedures give rise to defect structures which exhibit the same *g*-tensor characteristics, see, for example, refs 6 and 9, it is reasonable to assume that an intrinsic defect induces the symmetry reduction. Moreover, for reasons of charge compensation, a halide vacancy could be expected. As the *g*-tensor axes are tilted in the (110) plane, symmetry requires that the halide vacancy is located in this plane. In this work, we consider halide vacancies in the first three lattice shells, as illustrated in Figure 1.

Configurations with anion vacancies in the near vicinity of the central X^- ion are quite extended. As illustrated in paper 1, it is essential to take large parts of the system into account to properly incorporate lattice relaxations around the anion vacancy. To get a correct qualitative picture, the halide vacancy must be properly embedded quantum mechanically, whereas additional quantum or point charge embedding is required for accurate quantitative agreement.

An additional point of complexity in the current study is the fact that the *g*-tensor components deviate largely from the free electron value: $\Delta g = g - g_e$, ranging from 0.1 to 1.2. In literature, most ab initio calculations are restricted to *g* values showing a small deviation from the free electron value: Δg of the order ppt (10^{-3}). Only a limited number of theoretical works on systems with large *g* shifts (e.g., $\Delta g > 0.1$) are available on the other hand.[21−24] As a consequence, the quantum mechanical

* To whom correspondence should be addressed. E-mail: michel.waroquier@UGent.be. Tel: +32-9-264.65.59. Fax: +32-9-264.66.97.
[†] Laboratory for Theoretical Physics, Ghent University.
[‡] Department of Solid State Sciences, Ghent University.

10.1021/jp057010c CCC: $33.50
Published on Web 04/05/2006

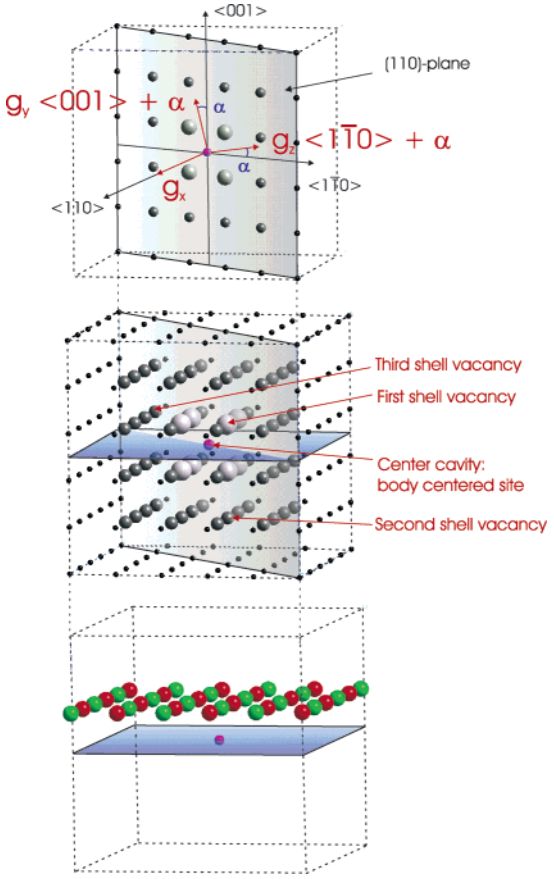

Figure 1. Definition of the used nomenclature for the X^- centers which exhibit monoclinic-I *g*-tensor symmetry. In the central figure, the 8 (largest spheres), 64 (intermediate spheres), and 216 (smallest spheres) atom clusters are illustrated. In the upper figure, the tilting angle α in the (110) plane is defined as the angle between the tensor axes and the ⟨001⟩ and ⟨1$\bar{1}$0⟩ directions. The position of the halide vacancy is the first three lattice shells indicated in the middle figure. Additionally, the positions of the alkali (green) and halide (red) atoms are defined in the lower part of the figure.

description of the defects under consideration is a great challenge for the present DFT methods.

The structure of the present work is as follows. In section 2, the computational details are summarized and the various clusters which are used in this work are introduced. In section 3, the defect model is first developed for the case study of KCl:S^- on which all theoretical modeling schemes are applied. Extension is made to all other MZ:X^- (M = Na, K, Rb and Z = Cl, Br) systems in section 4. The most important results are summarized in section 5.

2. Computational Details and Definition of Clusters

As already outlined in 1, various models can be applied for studying defects embedded in a crystal lattice. These can be merely classified into (i) cluster in vacuo, (ii) embedded cluster, and (iii) periodic calculations. For further details, we refer to 1.

Cluster in Vacuo Calculations. All cluster in vacuo calculations were performed using the Amsterdam Density Functional (ADF) program package, 2004.[25] Geometry optimizations were performed using a TZP (triple-ζ plus additional polarization function) basis set in combination with the VWN[26] functional. The subsequent EPR calculations in ADF were performed using the Bp86[27−28] functional form and a TZ2P (triple-ζ plus two polarization functions) basis set. These choices are motivated by an earlier level of theory study performed by the present authors on magnetic resonance parameters of diatomic chalcogen defects in alkali halides.[18] The relativistic atomic potentials were calculated using the auxiliary program DIRAC,[29] also comprised in the ADF package. For the calculation of *g* values, a spin−orbit relativistic restricted open shell approach has been used, while for the calculation of hyperfine couplings a scalar relativistic unrestricted approach, as both implemented in ADF, has been used. The frozen core approximation was applied for all ions (Na 2p, K 3p, Rb 3p, Cl 2p, and Br 3p) except for the central ion and the nearest alkali and halide ions.[16] In this notation, Na 2p means that all electrons up to the 2p electron shell were frozen.

TABLE 1: Composition and Definition of the Various Clusters Which Are Used for the Simulation of the X^- Centers Which Exhibit Monoclinic-I *g*-Tensor Symmetry[a]

cluster size	member	no. of atoms
8	($^1/_2$, $^1/_2$, $^1/_2$)	2 × 4
32	($^3/_2$, $^1/_2$, $^1/_2$)	2 × 12
56	($^3/_2$, $^3/_2$, $^1/_2$)	2 × 12
64	($^3/_2$, $^3/_2$, $^3/_2$)	2 × 4
88	($^5/_2$, $^1/_2$, $^1/_2$)	2 × 12
136	($^5/_2$, $^3/_2$, $^1/_2$)	2 × 24
160	($^5/_2$, $^3/_2$, $^3/_2$)	2 × 12
184	($^5/_2$, $^5/_2$, $^1/_2$)	2 × 12
208	($^5/_2$, $^5/_2$, $^3/_2$)	2 × 12
216	($^5/_2$, $^5/_2$, $^5/_2$)	2 × 4

[a] Each cluster is composed of all previous members. As reference, the body centered interstitial position, as defined in Figure 1, is used.

Embedded Cluster Calculations. Embedded cluster calculations were performed in Gaussian03,[30] as this package offers the possibility to optimize atomic positions in the quantum region within layers of point charges. Additionally, a three-layered embedding scheme was used, as implemented in the GUESS code[31−32] which has an interface with G03. For more details, we refer to 1. Similar to the ADF calculations, the VWN[26] functional form was used throughout all geometry optimizations and the Bp86[27−28] functional was again applied for all subsequent EPR calculations. A 6-31G** basis set[33] was used for all atoms of the lattice environment, while a 6-311G** basis set was applied for the central impurity ion.[18] For these calculations, Buckingham-type interatomic potentials, developed by van Beest et al.,[34−35] were used.

Periodic Calculations. The periodic calculations were performed within the CPMD code[36] which makes use of pseudopotentials and plane waves. The structures of the paramagnetic defects were optimized using a simulated annealing technique as proposed by Car and Parrinello.[37] Very soft pseudo-potentials of the Vanderbilt type including scalar relativistic corrections were used and an energy cutoff of 25 Ry (1 Ry = 1314 kJ/mol) was applied for the plane-wave expansion.[38] The electronic structure is described within the DFT formalism with use of the Bp86 gradient-corrected functional.[27−28]

2.1. Definition of Clusters. The definition of a lattice shell for an interstitial model differs from that in a substitutional model. In the latter, a lattice shell around a defect is composed of alkali or halide atoms (see paper 1). In the present study, the body centered interstitial position (ref 39) is taken as the center of the cluster (Figure 1). The shell composition and size of the various clusters, which are used in this work, are defined in Table 1. In Figure 1, the 8, 64, and 216 atoms clusters, which are perfect cubes, are illustrated. Each "member" of a given lattice shell, as defined in Table 1, contains both alkali and halide ions. In analogy with the substitutional class of defects, the

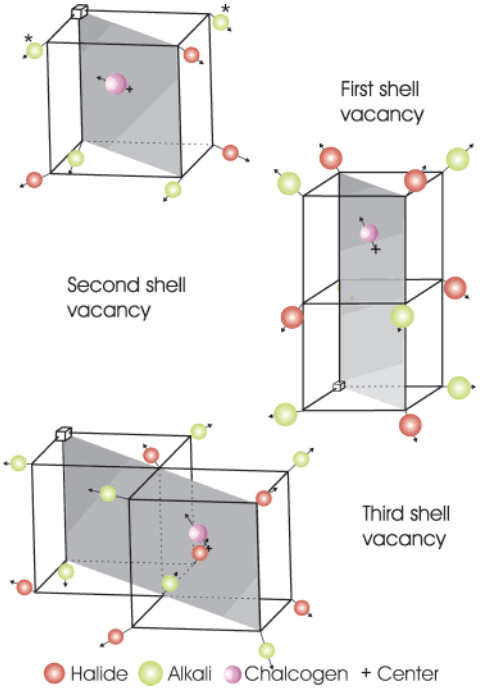

Figure 2. Illustration of the geometry relaxation of the nearest lattice environment of the KCl:S^- defect structure in the case of a halide vacancy in the first, second, and third lattice shells. The arrows indicate the direction of the relaxation. Additionally, the relaxed lattice positions are indicated. The cross (+) indicates the body centered site of the lattice.

various clusters used in this work are validated on their accuracy to reproduce relative energy differences and magnetic resonance parameters.

In the case of an interstitial defect structure, only one condition must be fulfilled for maintaining a given cluster, that is, the vacancy must fit into it. The charge neutrality requirement of the cluster and the reproduction of the Madelung potential at the defect site are fulfilled. From paper 1, we may also expect that proper embedding of the vacancy will be important. We will investigate this item for the case study KCl:S^- with monoclinic-I *g*-tensor symmetry using the aforementioned three simulation schemes and various cluster sizes.

Conform I, a compact notation, is introduced indicating the cluster size, the program package, and the approximation scheme that is used for the calculation. The general format is P(x_{QM}, x_{PI}, x_{PC}) where P stands for the program package that is used (ADF, G03, or CPMD), x_{QM} represents the number of atoms in the quantum region (layer I), x_{PI} is the number of polarizable ions (PI) in layer II, and x_{PC} is the number of fixed point charges (PC) in layer III. For cluster in vacuo and periodic calculations, the parameters x_{PI} and x_{PC} are all zero. In the following, this notation will be further clarified.

3. Case Study: KCl:S−

Nomenclature. As explained in the Introduction, it is reasonable to assume a halide vacancy in the vicinity of the defect ion. As the *g*-tensor axes are tilted in the (110) plane, symmetry requires that the halide vacancy is located in this plane. We consider halide vacancies in the first three lattice shells, as illustrated in Figures 1 and 2.

The KCl:S^- defect structure is taken as a test case for the three different simulation techniques. For the cluster in vacuo calculations, a cluster containing 216 atoms is used (the central X^- ion on the interstitial position is not counted), as it is the smallest cluster in which the vacancies under consideration are completely quantum mechanically embedded. All atoms which are not located at the edge of the cluster, that is, 64 atom positions, are allowed to relax. This model will be referred to as ADF(216,0,0).

TABLE 2: Binding Energy Difference (in eV) between the First Shell Vacancy (taken as reference) and the Second and Third Shell Vacancy Configurations, Using Three Simulation Techniques

vacancy	ADF(216,0,0)	G03(64,448,3584)	CPMD(216,0,0)
second shell		2.26	
third shell	1.69	2.31	1.84

For the embedded cluster calculations, a quantum cluster of 64 atoms is used (as illustrated in Figure 1) which is obtained by considering two cubic shells around the impurity ion. The second layer consists of two additional cubic shells, containing thus 512 − 64 = 448 atoms. The third layer contains 3584 fixed point charges or four additional cubic shells. We will refer to this approach as G03(64,448,3584).

For the periodic calculations, the unit cell contains 216 atoms, that is, being the smallest cubic box in which the vacancies are embedded in one quantum layer. The larger unit cell consisting of 512 lattice positions would not be computationally feasible. In these calculations, referred as CPMD(216,0,0), all atomic positions are allowed to relax.

Geometry Relaxation. The three simulation models are applied to study the geometry relaxation around the central S^- ion for the vacancy configurations under consideration. The obtained relaxations for the embedded cluster approach are illustrated in Figure 2. The arrows indicate the direction of the relaxation, and the final position of the relaxed lattice atoms is also indicated. Although the following discussion is mainly restricted to embedded cluster results, similar conclusions could be made for the cluster in vacuo and periodic approach.

The distortion of the nearest lattice environment of the S^- ion is a delicate interplay between the geometry relaxation induced by the S^- ion and the halide vacancy. For this reason, the geometry relaxation is only discussed qualitatively. All nearest lattice atoms of the S^- ion exhibit an outward relaxation with respect to the center of the interstitial cavity, independent of the position of the halide vacancy, which suggests that accommodation problems occur when the impurity ion is located in the interstitial cavity. As compared with the first shell vacancy relaxations, somewhat larger relaxations of the nearest lattice environment of the S^- ion are observed when the halide vacancy is located outside the first lattice shell. This suggests that a halide vacancy in the first shell, which enlarges the interstitial cavity, reduces the strain imposed on the cavity. The distance (2.69 Å) between S^- and the nearest K^+ ions (marked in Figure 2 with an asterisk) approximates the S−K distance calculated for KS (2.81 Å), K_2S (2.71 Å), and K_2S^+ (2.89 Å) in the gas phase. This may explain why the S^- ion is not located exactly in the middle of the interstitial cavity and does not relax completely to the vacancy.

Energetic Considerations. Apart from the geometrical considerations, the vacancy position that is energetically most favored will be preferred. In the three simulation schemes, the defect model with a first shell halide vacancy turns out to be by far the most bound. In Table 2, the energy differences (in electronvolts) with respect to this reference configuration are given. They are the result of intensive, high-demanding calculations with cluster sizes which are at the limit of present computer capacities. For the third shell vacancy, we tested the influence of the simulation model on the energetic results. The energy

TABLE 3: Comparison of Experimental and Computed *g* and Hyperfine Values for the KCl:S$^-$ Defect Structure Using the Cluster in Vacuo and Embedded Cluster Approach

	exp[a]	ADF(216,0,0)	G03(64,448,3584)
$g_{x,\langle 110\rangle}$	2.7665	2.7585	2.6458
$g_{y,\langle 001\rangle+\alpha}$	2.1502	2.1939	2.0854
$g_{z,\langle 1\bar{1}0\rangle+\alpha}$	1.7071	1.7505	1.8409
α	27.8	27.6	32.1
$A_{x,\langle 110\rangle}$	±143.3	159.9	138.5
$A_{y,\langle 001\rangle+\alpha}$	±103.5	102.9	−30.6
$A_{z,\langle 1\bar{1}0\rangle+\alpha}$	±101.7	96.3	−26.4
α	27.8	28.0	35.6

[a] Reference 9.

shows slight quantitative variations, but the overall qualitative picture does not change as the energy differences are very high. Vacancies in the second and third shell are higher in energy by almost 2 eV in the three schemes, giving evidence that the first shell vacancy configuration is energetically most favored. This conclusion is in agreement with geometrical findings discussed in the previous section.

On the basis of these structural and energetical results, the following defect model is proposed for the X$^-$ ions which exhibit monoclinic-I *g*-tensor symmetry: the X$^-$ ion is located in a double tetrahedral environment, with a first shell halide vacancy as a nearby perturbation.

EPR Parameters. The final validation of a defect model lies in its ability to reproduce the experimental EPR parameters. Computed *g* and hyperfine values, using the cluster in vacuo and embedded cluster approach, for the KCl:S$^-$ defect structure with a first shell halide vacancy are compared with the available experimental data (Table 3).

Qualitatively, all computed *g* and hyperfine values exhibit the correct behavior: the largest *g* and *A* values are observed along the ⟨110⟩ direction while the principal axes of the smallest and intermediate *g* and hyperfine values are tilted in the (110) plane. Excellent quantitative agreement between experimental and computed *g* and hyperfine values is obtained when using the cluster in vacuo technique. Moreover, the experimental tilting angle is perfectly reproduced by the latter method. The computed tilting angles for the *g* and hyperfine tensor axes are not coincident, but the difference is small.

These findings further promote the proposed defect model with a halide vacancy in the first lattice shell.

Selection of the Simulation Method. The final aim of this paper is to validate this defect model for the whole set of MCl:X$^-$ systems which exhibit monoclinic-I *g*-tensor symmetry. On the basis of the computational study performed on KCl:S$^-$ it may be concluded that the cluster in vacuo scheme using a 216 cluster (ADF(216,0,0)) gives the best agreement between experimental and theoretical EPR properties. Another important point concerns the fact that some lattices such as RbCl contain heavy lattice elements for which only a limited number of all-electron basis sets are available in Gaussian. The embedded cluster scheme, that is, the GUESS code, currently has an interface with G03 and is therefore less suited for the heavier elements. At this point, it is interesting to make note of the computational cost for the various schemes. Geometry optimization in the cluster in vacuo scheme (ADF(216,0,0)) requires approximately 1 month of CPU time on an ALTIX with 8 processors having each 2 GB of RAM. The subsequent EPR calculation takes an additional two weeks on the same configuration. To summarize, studying the eight systems of interest at the ADF(216,0,0) level would require approximately 1 year of computer time on the aforementioned systems.

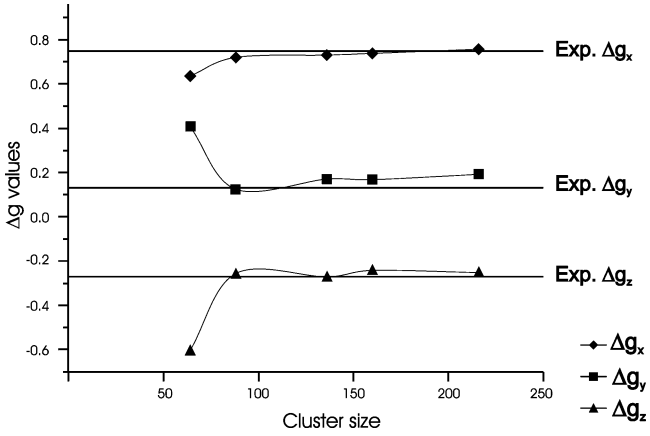

Figure 3. Influence of cluster size effects on the computed Δ*g* values for the KCl:S$^-$ defect structure, using the cluster in vacuo approach. The experimental values are indicated by full lines.

In view of this, we investigate the use of a computationally attractive scheme for the other systems but without loss of qualitative and quantitative agreement. When maintaining the condition of full cubic shells around the X$^-$ ion, clusters of 64, 216, 512, etc., atoms, may be retained. In the case of a 64-atom cluster with a first shell vacancy, only one quantum layer surrounds the vacancy. It must be verified whether such an approach gives acceptable qualitative results for the *g* tensor. For completeness of the study, calculations have also been performed on clusters containing 88, 136, and 160 atoms (Table 1). These clusters still fulfill the required symmetry conditions but do not consist of complete cubic cells around the X$^-$ ion. These approaches are labeled as ADF(64,0,0), ADF(88,0,0), ADF(136,0,0), ADF(160,0,0), and ADF(216,0,0) in the following discussion. Prior to the EPR calculations, all atoms which were not located at the edge of the cluster were allowed to relax. The influence of the cluster size on the computed *g* values is presented in Figure 3. Convergence is reached from the 88-atom cluster for all *g*-tensor components.

Taking into account the fact that the systems under study exhibit very large deviations from the free electron value (Δ*g*: $-0.3 \rightarrow 0.8$), we may conclude that we succeed in a very good quantitative reproduction of the *g* tensor. To the best of our knowledge, systems characterized with such large Δ*g* values were never computationally studied until now, except for previous work of the authors on diatomic defects.[15−18]

In view of the computational cost, we may easily reduce the dimension of the cluster to 88 atoms without losing a lot of accuracy. For the further exploration of the MCl:X$^-$ defect structures, we will therefore apply the ADF(88,0,0) approach, motivated by the substantial reduction of computational cost and the availability of accurate basis sets in ADF also for the heavier elements.

4. EPR Parameters of X− Ions with Monoclinic-I *g*-Tensor Symmetry

Through the use of the proposed defect model and simulation scheme, the EPR parameters of all other MCl:X$^-$ (M = Na, K, Rb) defect structures with monoclinic-I *g*-tensor symmetry are calculated. The results are listed in Table 4.

Taking into account the large deviations of the principal *g* values from the free electron value, the quantitative agreement between experimental and calculated *g* values is excellent for all defect structures. However, in all cases, the experimental g_x and g_y values are somewhat underestimated theoretically, while the g_z value is systematically overestimated. The largest

TABLE 4: Experimental and Calculated *g* Values and Hyperfine Data (in MHz) for Monoatomic Chalcogen Centers with Monoclinic-I *g*-Tensor Symmetry[a]

	exp				theor			
	$g_{x,\langle 110\rangle}$	$g_{y,\langle 001\rangle+\alpha}$	$g_{z,\langle 1\bar{1}0\rangle+\alpha}$	α	$g_{x,\langle 110\rangle}$	$g_{y,\langle 001\rangle+\alpha}$	$g_{z,\langle 1\bar{1}0\rangle+\alpha}$	α
KCl:O^- [b]	2.4524	2.2217	1.9475	12.5	2.4166	2.1217	1.9982	11.7
RbCl:O^- [b]	2.5330	2.2344	1.9154	12.5	2.5034	2.1096	1.9989	10.2
KBr:O^- [b]	2.4416	2.2346	1.9508	n.a.	2.4699	2.2936	1.8652	1.2
NaCl:S^- [c]	2.3602	2.2700	1.9574	14.2	2.3021	2.1914	1.9904	15.1
KCl:S^- [c]	2.7665	2.1502	1.7071	27.8	2.7219	2.1269	1.7462	28.2
RbCl:S^- [d]	2.9318	1.9240	1.5090	32.7	2.8866	1.8650	1.6664	33.5
NaCl:Se^- [e]	2.6670	2.3453	1.7279	8.2	2.5885	2.3043	1.8122	8.9
RbCl:Se^- [f]	3.2648	1.4558	1.1090	19.4	3.0402	1.3285	1.2369	22.4
	A_x	A_y	A_z		A_x	A_y	A_z	
KCl:O^- [b]	n.a.	n.a.	n.a.	n.a.	64.3	63.3	−216.7	8.6
RbCl:O^- [b]	<125	< 50	−210.0	12.5	70.1	68.9	−215.7	11.1
KBr:O^- [b]	80.3	< 75	−214.5	n.a.	86.9	70.4	−210.3	1.8
NaCl:S^- [c]	−55.2	−46.9	131.2	14.2	−22.0	−20.8	126.8	14.9
KCl:S^- [c]	143.3	103.5	101.7	27.8	152.8	88.7	81.0	26.0
RbCl:S^- [d]	n.a.	n.a.	n.a.	n.a.	173.7	−58.3	−55.9	32.2
NaCl:Se^- [e]	615.8	484.5	425.5	8.2	587.2	466.4	447.8	13.5
RbCl:Se^- [f]	1050.5	437.0	297.0	19.4	985.3	412.5	300.2	21.3

[a] For all structures, a first shell halide vacancy was considered. The tilting angle of the principal *g*-tensor axes in the (110) plane is defined as α. Because the tilting angles of the hyperfine tensor axes could not be exactly determined experimentally, the same values as those for the *g*-tensor axes were proposed. [b] Reference 6. [c] Reference 9. [d] Reference 12. [e] Reference 11. [f] Reference 10.

deviations from experiment are observed for the RbCl:Se^- defect structure: an absolute deviation of 225 ppt or smaller. Nevertheless, because very large deviations from the free electron value occur in this case, $\Delta g \approx 1.2$, the agreement with experiment can still be regarded as highly satisfactory.

Next to the excellent description of the *g* tensor, the calculations perfectly reproduce the experimental hyperfine coupling constants. For those defect structures where comparison with experimental data can be made, excellent quantitative agreement is obtained. The signs of these couplings could not be determined experimentally. For this reason, the signs of the experimental values have been adjusted according to the theoretical predictions.

The correspondence between the calculated and observed tilting of the principal g_y and g_z axes in the (110) plane is striking. We note however that the computed tilting angles of the *g* and hyperfine tensors are not coincident, although the deviations are small. Such a noncoincidence is not expected to be resolved experimentally.

Previous results also underline some remarkable trends. For all defect structures, the experimental g_y value is larger than g_e, except for the RbCl:S^- and Se^- defect structures. The calculations confirm these observations.

For the NaCl:S^- and KCl:S^- defect structures, it is observed experimentally and reproduced computationally that the hyperfine tensor is nearly axial along the $\langle 1\bar{1}0\rangle + \alpha$ and $\langle 110\rangle$ directions, respectively. For the RbCl:S^- defect structure, the calculations predict that the hyperfine tensor is again nearly axial along the $\langle 110\rangle$ direction, as for KCl, but different signs are obtained for the $A_\perp$ values.

In Figure 4, the experimental and theoretical g_x value and the tilting angle α in the (110) plane are plotted as a function of the lattice constant. For the g_y and g_z values, a similar plot can be made. When the alkali ion is englarged for a fixed X^- defect, the following dependencies are noticed experimentally and reproduced theoretically: the principal g_x value and tilting angle increase and the principal g_y and g_z values decrease. The latter dependencies are reproduced correctly by the calculations.

KBr:O^- Case. Because a similar doping procedure was used for the KBr:O^-, KCl:O^-, and RbCl:O^- defect structures, it was

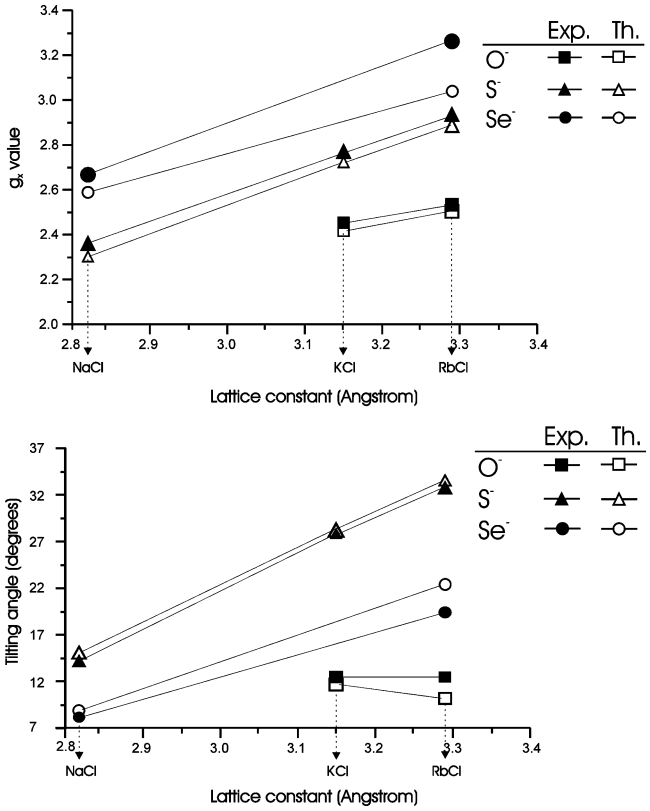

Figure 4. Experimental and computed g_x value and tilting angle α as a function of the lattice environment.

suggested from experiment[6] that these centers are of the same nature. Because a substitutional model with a nearest neighbor halide vacancy failed to describe the KBr:O^- center (see paper 1), this center is now investigated using the interstitial defect model. As can be concluded from the results reported in Table 4, the calculations perfectly reproduce the experimental principal *g* and hyperfine values using the interstitial defect model. Therefore, we assign the KBr:O^- center to the class of defects which exhibits monoclinic-I *g*-tensor symmetry, with a tilting angle which is too small to be resolved experimentally.

5. Conclusion

The present paper finalizes the search for suitable defect models for the X^- centers in alkali halides. In a previous paper (1), attention was focused on X^- centers which were located on a substitutional lattice position. In this paper, we investigated X^- ions which occur interstitially. In the following, we summarize the most important results of the present work.

All X^- defects under consideration exhibited monoclinic-I *g*-tensor symmetry. Experimentally, it was suggested that the X^- ion was located on an interstitial position with a nearby perturbation. Because different doping procedures gave rise to defect structures which exhibited the same *g*-tensor characteristics, we suggested a halide vacancy as perturbation. On the $KCl:S^-$ test case, the influence of the position of the halide vacancy on the geometry relaxation and relative energy was investigated using three simulation schemes (cluster in vacuo, embedded cluster, and periodic). Additionally, EPR calculations were performed using various schemes and different cluster sizes. The proposed defect model for the X^- ions which exhibit monoclinic-I *g*-tensor symmetry can be summarized as follows: the X^- ion is located in a double tetrahedral environment, with a first shell halide vacancy as a nearby perturbation. By the use of the latter defect model, EPR parameters of all other $MCl:X^-$ centers were calculated. In all cases, excellent agreement with experiment was obtained. Additionally, for the O^- center with (nearly) orthorhombic-I symmetry in KBr, it was validated that the interstitial defect model was able to reproduce the experimental data.

As a general conclusion, we can state that X^- ions in alkali halides are fully characterized. A clear distinction between substitutional and interstitial X^- ions was made and suitable defect models were proposed for all X^- centers. In all these models, the X^- ion is accompanied by a halide vacancy and we verified that in each case the energetically favored configuration is experimentally encountered. The occurrence of X^- ions in substitutional or interstitial positions is most probably related to the chemical details of the doping and the resulting formation of X^{2-} precursors.

Acknowledgment. The authors (in particular V.V.S., H.V., and E.P.) would like to thank the Fund for Scientific Research (FWO-Flanders, Belgium) for financial support. The Research board of Ghent University is also gratefully acknowledged.

References and Notes

(1) Wu, J.; Lin, J. *J. Cryst. Growth* **2002**, *240*, 495.
(2) Nishidate, K.; Baba, M.; Sarjono, S.; Hasegawa, M.; Nishikawa, K.; Sokolska, I.; Ryba-Romanowski, W. *Phys. Rev. B* **2003**, *68*, 224307.
(3) Sarjono, S.; Baba, M.; Nishidate, K.; Ohta, K.; Sokolska, I.; Ryba-Romanowski, W. *Jpn. J. Appl. Phys.* **2004**, *43*, 3461.
(4) Känzig, W.; Cohen, M. H. *Phys. Rev. Lett.* **1959**, *3*, 509.
(5) Vannotti, E.; Morton, J. R. *Phys. Rev.* **1968**, *174*, 448.
(6) Brailsford, J. R.; Morton, J. R. *J. Chem. Phys.* **1969**, *51*, 4794.
(7) Matthys, P.; Callens, F.; Boesman, E. *Solid State Commun.* **1983**, *45*, 1.
(8) Callens, F.; Matthys, P.; Boesman, E. *Phys. Status Solidi B* **1983**, *118*, K35.
(9) Callens, F.; Maes, F.; Matthys, P.; Boesman, E. *J. Phys.: Condens. Matter* **1989**, *1*, 6921.
(10) Matthys, P.; Maes, F.; Callens, F.; Boesman, E. *Solid State Commun.* **1990**, *75*, 17.
(11) Maes, F.; Callens, F.; Matthys, P.; Boesman, E. *J. Phys. Chem. Solids* **1990**, *51*, 1289.
(12) Maes, F.; Callens, F.; Matthys, P.; Boesman, E. *Radiat. Eff. Defects Solids* **1991**, *116*, 283.
(13) Van Doorslaer, S.; Callens, F.; Maes, F.; Boesman, E. *Phys. Rev. B* **1996**, *54*, 1145.
(14) Van Doorslaer, S.; Maes, F.; Callens, F.; Matthys, P.; Boesman, E. *J. Chem. Soc., Faraday Trans.* **1996**, *92*, 1579.
(15) Stevens, F.; Vrielinck, H.; Callens, F.; Pauwels, E.; Waroquier, M. *Phys. Rev. B* **2002**, *66*, 134103.
(16) Stevens, F.; Vrielinck, H.; Callens, F.; Pauwels, E.; Waroquier, M. *Phys. Rev. B* **2003**, *67*, 104429.
(17) Stevens, F.; Vrielinck, H.; Callens, F.; Waroquier, M. *Solid State Commun.* **2004**, *132*, 787.
(18) Stevens, F.; Van Speybroeck, V.; Pauwels, E.; Vrielinck, H.; Callens, F.; Waroquier, M. *Phys. Chem. Chem. Phys.* **2005**, *7*, 240.
(19) Van Speybroeck, V.; Pauwels, E.; Stevens, F.; Callens, F.; Waroquier, M. *Int. J. Quantum Chem.* **2005**, *101*, 761.
(20) Stevens, F.; Vrielinck, H.; Callens, F.; Pauwels, E.; Van Speybroeck, V.; Waroquier, M. *Int. J. Quantum Chem.* **2005**, *102*, 409.
(21) Alvares-Thon, L.; Hernandez-Acevedo, L.; Arratia-Perez, R. *J. Chem. Phys.* **2001**, *115*, 726.
(22) Foerster, S.; Stein, M.; Brecht, M.; Ogata, H.; Higuchi, Y.; Lubitz, Y. *J. Am. Chem. Soc.* **2002**, *125*, 83.
(23) Arratia-Perez, R.; Hernandez-Acevedo, L. *J. Chem. Phys.* **2003**, *118*, 7425.
(24) Brownridge, S.; Grein, F. *J. Phys. Chem. A* **2003**, *107*, 7969.
(25) ADF, http://tc.chem.vu.nl/SCM., Department of Theoretical Chemistry, Vrije Universiteit Amsterdam.
(26) Vosko, S. H.; Wilk, L.; Nusair, M. *Can. J. Phys.* **1980**, *58*, 1200.
(27) Becke, A. D. *Phys. Rev. A* **1988**, *28*, 3098.
(28) Perdew, J. P. *Phys. Rev. B* **1986**, *33*, 8822.
(29) Herman, F.; Skilman, F. *Atomic Structure Calculations*; Prentice-Hall: Engelwood Cliffs, NJ, 1963.
(30) Frisch, M. J.; Trucks, G. W.; Schlegel, H. B.; Scuseria, G. E.; Robb, M. A.; Cheeseman, J. R.; Montgomery, J. A., Jr.; Vreven, T.; Kudin, K. N.; Burant, J. C.; Millam, J. M.; Iyengar, S. S.; Tomasi, J.; Barone, V.; Mennucci, B.; Cossi, M.; Scalmani, G.; Rega, N.; Petersson, G. A.; Nakatsuji, H.; Hada, M.; Ehara, M.; Toyota, K.; Fukuda, R.; Hasegawa, J.; Ishida, M.; Nakajima, T.; Honda, Y.; Kitao, O.; Nakai, H.; Klene, M.; Li, X.; Knox, J. E.; Hratchian, H. P.; Cross, J. B.; Adamo, C.; Jaramillo, J.; Gomperts, R.; Stratmann, R. E.; Yazyev, O.; Austin, A. J.; Cammi, R.; Pomelli, C.; Ochterski, J. W.; Ayala, P. Y.; Morokuma, K.; Voth, G. A.; Salvador, P.; Dannenberg, J. J.; Zakrzewski, V. G.; Dapprich, S.; Daniels, A. D.; Strain, M. C.; Farkas, O.; Malick, D. K.; Rabuck, A. D.; Raghavachari, K.; Foresman, J. B.; Ortiz, J. V.; Cui, Q.; Baboul, A. G.; Clifford, S.; Cioslowski, J.; Stefanov, B. B.; Liu, G.; Liashenko, A.; Piskorz, P.; Komaromi, I.; Martin, R. L.; Fox, D. J.; Keith, T.; Al-Laham, M. A.; Peng, C. Y.; Nanayakkara, A.; Challacombe, M.; Gill, P. M. W.; Johnson, B.; Chen, W.; Wong, M. W.; Gonzalez, C.; Pople, J. A. *Gaussian 03*, revision B.3; Gaussian, Inc.: Pittsburgh, PA, 2003.
(31) Sushko, P. V.; Shluger, A. L.; Catlow, C. R. A. *Surf. Sci.* **2000**, *450*, 153.
(32) Sushko, P. V.; Shluger, A. L.; Baetzold, R. C.; Catlow, C. R. A. *J. Phys.: Condens. Matter* **2000**, *12*, 8257.
(33) Rassolov, V.; Pople, J. A.; Ratner, M.; Windus, T. L. *J. Chem. Phys.* **1998**, *109*, 1223.
(34) van Beest, B. W. H.; Kramer, G. J.; Santen, R. A. *Phys. Rev. Lett.* **1955**, *64*, 8.
(35) Sushko, P. V.; Mukhopadhyay, S.; Mysovsky, A. S.; Sulimov, V. B.; Taga, A.; Shluger, A. L. *J. Phys.: Condens. Matter* **2005**, *17*, S2115.
(36) Hutter, J.; Ballone, P.; Bernasconi, M.; Focher, P.; Fois, E.; Goedecker, S.; Parrinello, M.; Tuckermann, M. E. CPMD, V3.7, Copyright IBM Corp, 1990−2003, Copyright MPI fuer Festkoerperforschung Stuttgart, 1997−2001.
(37) Car, R.; Parrinello, M. *Phys. Rev. Lett.* **1985**, *55*, 2471.
(38) Vanderbilt, D. *Phys. Rev. B* **1990**, *41*, 7892.
(39) Stoneham, A. M. *Theory of Defects in Solids*; Clarendon Press: Oxford, U.K., 1975.